Unified discontinuous Galerkin finite-element framework for transient conjugated radiation-conduction heat transfer

Cun-Hai Wang ⬤,* Xiao-Yang Zhang, Chong-Chao Pan ⬤, and Ze-Yi Jiang

School of Energy and Environmental Engineering, University of Science and Technology Beijing, Beijing 100083, China

Research on conjugated radiation-conduction (CRC) heat transfer in participating media is of vital scientific and engineering significance due to its extensive applications. Appropriate and practical numerical methods are essential to forecast the temperature distributions during the CRC heat-transfer processes. Here, we established a unified discontinuous Galerkin finite-element (DGFE) framework for solving transient CRC heat-transfer problems in participating media. To overcome the mismatch between the second-order derivative in the energy balance equation (EBE) and the DGFE solution domain, we rewrite the second-order EBE as two first-order equations and then solve both the radiative transfer equation (RTE) and the EBE in the same solution domain, resulting in the unified framework. Comparisons between the DGFE solutions with published data confirm the accuracy of the present framework for transient CRC heat transfer in one- and two-dimensional media. The proposed framework is further extended to CRC heat transfer in two-dimensional anisotropic scattering media. Results indicate that the present DGFE can precisely capture the temperature distribution at high computational efficiency, paving the way for a benchmark numerical tool for CRC heat-transfer problems.

I. INTRODUCTION

Research on gaining highly accurate solutions for conjugated radiation-conduction (CRC) heat-transfer problems has sparked increasing research interest in recent years due to its extensive applications in engineering, including semitransparent media [1], porous material [2], fibrous insulation [3], and ceramics insulation [4]. The CRC heat-transfer problems are controlled by the energy balance equation (EBE) coupled with the radiative transfer equation (RTE). The RTE is an intricate integral-differential equation, for which it is almost impossible to obtain analytical solutions for general cases. In addition, the radiation serves as a source term in the EBE [5], leading to solid nonlinearity of the EBE. Thus, numerical methods have become the mainstream for handling CRC heat-transfer problems.

Various numerical methods have been successfully utilized to solve CRC heat-transfer problems in participating media. In the early 1960s, by using a direct iterative algorithm, Viskanta *et al.* [6,7] first acquired the approximate solutions to steady-state CRC heat-transfer problems in parallel slabs filled with an emitting and absorbing medium. However, this iterative method requires too much time to reach convergence because of the complexity of the governing equation, and it cannot extend to transient or multidimensional cases. Due to the significant directionality nature of the RTE, some scholars used some special methods to solve it, and then they coupled the radiation information into the EBE by using conventional computational algorithms. For instance, Talukdar *et al.* [8] addressed the radiative part of CRC problems in

a one-dimensional (1D) absorbing, emitting, and anisotropic scattering medium by using the collapsed dimension method (CDM), and they applied the Crank-Nicholson difference scheme for the discretization of the EBE. Mishra *et al.* [9–11] obtained the radiation information by the discrete transfer method (DTM), the finite-volume method (FVM), and the discrete ordinate method (DOM), respectively, and they used a lattice Boltzmann method (LBM) to solve the EBE in planar and rectangular geometries. Although these numerical methods can be used to obtain accurate radiation information, the drawback of hybrid methods is that the mesh incompatibility problem usually occurs, resulting in additional node interpolations. Thus, some researchers tried to build unified numerical methods for both the RTE and the EBE. For example, Razzaque *et al.* [12] employed the finite-element method (FEM) in solving the CRC heat-transfer problems in a rectangular enclosure. Zhao *et al.* [13] proposed a spectral element method (SEM) to solve the steady CRC heat-transfer problems in 1D and 2D semitransparent media. Wei *et al.* [14] investigated the radiation effects on the temperature distribution in a rectangular semitransparent medium via a unified LBM. These unified methods show good geometric adaptability and ease of coding, but the computational cost is huge for multidimensional cases. All the above numerical methods are based on the mesh discretization of the spatial domain. In contrast, Zhang *et al.* [15] proposed a meshless nature element method (NEM) for the numerical calculations of CRC problems. Nevertheless, the calculation quantity of the NEM is very large due to the complicated shape functions.

Pioneered by Reed and Hill [16], the discontinuous finite-element method (DFEM) has many attractive advantages, such as local conservation, geometric flexibility, and high parallel efficiency [17]. The DFEM was originally used to solve

---

*Corresponding author: wangcunhai@ustb.edu.cn

hyperbolic conservation law equations, and it has achieved significant success in many flow and heat-transfer fields [18–21]. As for the applications of the DFEM in solving the RTE, Cui and Li [22,23] carried out the first attempt at the beginning of this century. They adopted a standard upwind numerical flux and applied the DFEM to solve the internal radiation problems. Later, Liu *et al.* [24] extended the DFEM to radiative problems in 2D semitransparent media with graded index distributions. Kitzmann *et al.* [25] presented a DFEM to solve the RTE in a spherical and symmetric structure with arbitrary scattering phase functions. Clarke *et al.* [26] used high-order polynomials for space and angular discretization, and they discussed the DFEM convergence for radiative transfer problems under different boundary conditions. Their results showed that the DFEM could achieve a $p + 1$ convergence rate using a polynomial of degree p. Feng *et al.* [27] utilized the DFEM with a local numerical flux scheme for radiative transfer problems with strong inhomogeneity. Although the DFEM has been proven effective and accurate for pure radiation problems, there has been much less progress regarding its applications to CRC heat-transfer problems.

By using a high-order DFEM for the RTE and a continuous FEM for solving the EBE, respectively, Ghattassi *et al.* [28] studied the combined radiation-conduction characteristics under the Dirichlet and Robin boundary conditions. Their results showed that the DFEM could easily couple with other numerical methods with good numerical stability. Wang *et al.* [29] investigated the CRC heat-transfer problems in irregular media by the DFEM with an upwind numerical flux. But in their work, the calculation cannot be implemented element by element, which seriously impedes the computation efficiency. Although it is convenient to discretize the EBE by using the FEM, the FEM cannot accurately capture the temperature distribution in the cases involving strong temperature inhomogeneity or discontinuity, such as in the multilayered thermal protective coatings for high-temperature aircraft skin. In such scenarios, the DFEM is necessary for predicting and capturing the temperature distribution with strong fluctuations.

In practice, the main hindrance of DFEM extension to CRC heat-transfer problems lies in the mismatch between the DFEM solution domain and the second-order derivative in the EBE. To overcome this mismatch, Cockburn and Shu [30,31] rewrote the second-order equation as two first-order equations by introducing an auxiliary variable, they implemented DFEM discretization like that for a hyperbolic equation, and then they proposed a local discontinuous Galerkin (DG) method integrating with the advantages of local solvability and optimal convergence. However, current studies on the local DG method mainly focus on its convergence characteristics with specifically defined periodic boundary conditions [32]. To the best of our knowledge, a unified DGFE framework where both the RTE and EBE are discretized via the DG scheme for CRC heat-transfer problems is still lacking.

This work aims to establish a unified DGFE framework for transient CRC heat-transfer problems. The governing equations and corresponding DGFE discretization are presented in Sec. II, followed by a detailed solution procedure of the proposed framework. In Sec. III, the capability of the present framework for CRC heat-transfer problems is first verified by comparing the DGFE solutions with published data for 1D and 2D cases. Finally, in Sec. IV, the work is summarized.

II. MATHEMATICAL MODEL

A. Governing equation

For the transient CRC heat-transfer problems in a participating medium, the EBE is written as [33]

$$\rho c_p \frac{\partial T(\mathbf{r})}{\partial t} = k\nabla^2 T(\mathbf{r}) - \nabla \cdot \mathbf{q}_\mathrm{r}(\mathbf{r}),\qquad(1)$$

where T is the temperature; t is the time; $\mathbf{r}$ is the position coordinate; ρ, c_p, and k are the density, specific heat, and thermal conductivity of the medium, respectively; and $\nabla \cdot \mathbf{q}_\mathrm{r} = \frac{\partial q_{r,x}}{\partial x} + \frac{\partial q_{r,y}}{\partial y}$ is the divergence of radiative heat flux [see Fig. 1(a)] obtained from

$$\nabla \cdot \mathbf{q}_\mathrm{r}(\mathbf{r}) = \beta(1 - \omega)\left(4\sigma T^4(\mathbf{r}) - \int_{4\pi} I(\mathbf{r}, \mathbf{\Omega})d\mathbf{\Omega}\right),\quad(2)$$

where $\beta = \kappa_\mathrm{a} + \kappa_\mathrm{s}$ is the extinction coefficient, with κ_a and κ_s denoting the absorption coefficient and scattering coefficient, respectively, $\omega = \kappa_\mathrm{s}/\beta$ is the scattering albedo, σ is the Stefan-Boltzmann constant $(5.67 \times 10^{-8}\,\mathrm{W\,m^{-2}\,K^{-4}})$, I is the radiation intensity, $\mathbf{\Omega}(\theta, \varphi)$ is the radiative direction angle with θ and φ denoting the zenith and azimuth angle, respectively, seen in Fig. 1(b), and $\mathbf{q}_\mathrm{r}$ is the radiative heat flux calculated via

$$\mathbf{q}_\mathrm{r} = \int_{4\pi} I(\mathbf{r}, \mathbf{\Omega})\hat{s}d\mathbf{\Omega},\qquad(3)$$

where $\hat{s}$ denotes the direction cosine of $\mathbf{\Omega}$.

The discrete-ordinate form of the RTE is written as [33]

$$\mathbf{\Omega}^m \cdot \nabla I(\mathbf{r}, \mathbf{\Omega}^m) + \beta I(\mathbf{r}, \mathbf{\Omega}^m) = S(\mathbf{r}, \mathbf{\Omega}^m),\qquad(4)$$

where S is the source term given by

$$S(\mathbf{r}, \mathbf{\Omega}^m) = \kappa_\mathrm{a}I_\mathrm{b}(\mathbf{r}, \mathbf{\Omega}^m) + \frac{\kappa_\mathrm{s}}{4\pi}\sum_{m'=1}^{M} I(\mathbf{r}, \mathbf{\Omega}^{m'})\Phi(\mathbf{\Omega}^{m'}, \mathbf{\Omega}^m)w^{m'},$$
$$(5)$$

where I_b is the blackbody radiation intensity, $M = N_\theta \times N_\varphi$ is the total number of discrete directions with N_θ and N_φ denoting the discrete directions in the zenith and azimuth space, respectively, $m = 1, 2, \ldots, M$ is the direction index, and w is the weight of each discrete angle. $\Phi(\mathbf{\Omega}^{m'}, \mathbf{\Omega}^m)$ is the scattering phase function defined as

$$\Phi(\mathbf{\Omega}^{m'}, \mathbf{\Omega}^m) = \frac{I_\mathrm{s}(\mathbf{\Omega}^{m'}, \mathbf{\Omega}^m)}{\frac{1}{4\pi}\int_{4\pi} I_\mathrm{s}(\mathbf{\Omega}^{m'}, \mathbf{\Omega}^m)d\mathbf{\Omega}^m},\qquad(6)$$

with $I_\mathrm{s}(\mathbf{\Omega}^{m'}, \mathbf{\Omega}^m)$ denoting the direction scattering intensity.

For the opaque wall, the diffuse reflective boundary condition of the RTE is given by

$$I_\mathrm{w}(\mathbf{r}_\mathrm{w}, \mathbf{\Omega}^m) = \varepsilon_\mathrm{w}I_\mathrm{bw}(\mathbf{r}_\mathrm{w})$$
$$+ \frac{1 - \varepsilon_\mathrm{w}}{\pi}\sum_{\mathbf{n}_\mathrm{w}\cdot\mathbf{\Omega}^{m'}<0} I_\mathrm{w}(\mathbf{r}_\mathrm{w}, \mathbf{\Omega}^{m'})|\mathbf{n}_\mathrm{w}\cdot\mathbf{\Omega}^{m'}|w^{m'},$$
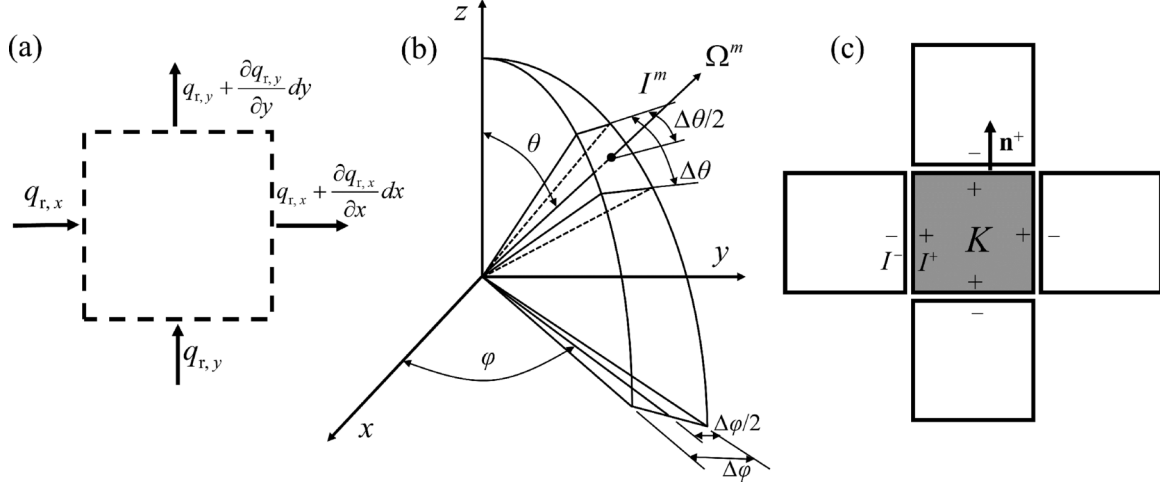$$(7)$$

FIG. 1. Schematic diagrams of (a) the physical meaning of divergence of radiative heat flux, (b) radiation intensity I^m and radiative direction angle Ω^m, and (c) relations of variable values.

where ε_w denotes the wall emissivity and $\mathbf{n}_\mathrm{w}$ denotes the unit inward normal vector of the boundary.

B. DGFE discretization for the RTE

For the sake of conciseness and without introducing any ambiguity, the terms $I(\mathbf{r}, \mathbf{\Omega}^m)$ and $S(\mathbf{r}, \mathbf{\Omega}^m)$ are replaced by I^m and S^m, respectively. Then Eq. (4) is written as

$$\mathbf{\Omega}^m \cdot \nabla I^m + \beta I^m = S^m. \tag{8}$$

By multiplying the weight function W on both sides of Eq. (8) and integrating by the Gauss divergence theorem in the element K, we can get the weak form of Eq. (8) as

$$\int_{\partial K} \widehat{\mathbf{\Omega}^m I^m} \cdot \mathbf{n}^+ \cdot W \, dl - \int_K I^m \mathbf{\Omega}^m \cdot \nabla W \, dA + \int_K \beta I^m W \, dA$$
$$= \int_K S^m W \, dA, \tag{9}$$

where $\int_{\partial K}$ is the line integral over the edge of element K, $\int_K$ is the surface integral over element K, $\mathbf{n}^+$ is the unit outward normal vector of the element edge, and $\widehat{\mathbf{\Omega}^m I^m}$ is the numerical flux. In this paper, a local Lax-Friedrichs numerical flux scheme [34] where the angular direction vectors are separated from the spatial coordinates is applied, and the numerical flux is written as

$$\widehat{\mathbf{\Omega}^m I^m} = \mathbf{\Omega}^m \{I^m\} + |\mathbf{\Omega}^m|[I^m]\mathbf{n}^+, \tag{10}$$

where $\{I^m\}$ and $[I^m]$ are the average and jump of I^m on the two sides of the element edge, respectively, and they are written as

$$\{I^m\} = \tfrac{1}{2}(I^{m^+} + I^{m^-}), \quad [I^m] = \tfrac{1}{2}(I^{m^+} - I^{m^-}), \tag{11}$$

where I^{m^+} is the radiation intensity on the edge in the element K, and I^{m^-} is that on its neighbor edge, as seen in Fig. 1(c). For the boundary-connected elements, the numerical flux is written as

$$\widehat{\mathbf{\Omega}^m I^m} = \widehat{\mathbf{\Omega}^m I^m_\mathrm{w}}. \tag{12}$$

Then substitute Eqs. (10) and (11) into Eq. (9), and utilize the Galerkin weighting scheme where the weight function W

is chosen as the shape function ϕ_i which is selected as the one-order linear polynomial [13]. One gets the second-order convergent DGFE discretization of the RTE in the matrix form as

$$\mathbf{K}^m \mathbf{I}^m = \mathbf{H}^m, \tag{13}$$

where $\mathbf{I}^m = [I^m_1, I^m_2, \ldots, I^m_n]^\mathrm{T}$ is the radiation intensity on the solution nodes in one element, with n denoting the node number. The matrix elements in the stiffness matrix $\mathbf{K}$ and the column vector $\mathbf{H}$ are calculated by

$$\mathbf{K}_{ji} = -\int_K \phi_i \mathbf{\Omega}^m \cdot \nabla \phi_j \, dA + \frac{1}{2} \int_{\partial K} (\mathbf{\Omega}^m \cdot \mathbf{n}^+ + |\mathbf{\Omega}^m|)\phi_i \phi_j \, dl$$
$$+ \int_K \beta \phi_i \phi_j \, dA, \tag{14}$$

$$\mathbf{H}_j = \sum_{i=1}^n \int_K S^m_i \phi_i \phi_j \, dA - \frac{1}{2} \sum_{i=1}^n \int_{\partial K} (\mathbf{\Omega}^m \cdot \mathbf{n}^+ - |\mathbf{\Omega}^m|)$$
$$\times I^{m^-}_i \phi_i \phi_j \, dl, \tag{15}$$

where ϕ_i and ϕ_j are the weight functions, and the subscripts i and j represent the index for column and row, respectively.

C. DGFE discretization for EBE

The brackets in Eq. (1) are omitted for the convenience of deducing the discretization equation. Then Eq. (1) is abbreviated as

$$\rho c_p \frac{\partial T}{\partial t} = k \nabla^2 T - \nabla \cdot \mathbf{q}_\mathrm{r}. \tag{16}$$

Based on the main idea of the local DG scheme, an auxiliary variable $\mathbf{q} = [q_x, q_y]^\mathrm{T}$ needs to be introduced to rewrite Eq. (16) into two first-order equations [31], that is,

$$\mathbf{q} = k \nabla T, \tag{17}$$

$$\rho c_p \frac{\partial T}{\partial t} = \nabla \cdot \mathbf{q} - \nabla \cdot \mathbf{q}_\mathrm{r}. \tag{18}$$

Similarly, Eqs. (17) and (18) are multiplied by the weight functions $\mathbf{w}$ and v, respectively, and integrated by the Gauss divergence theorem in the element K. Then the weak forms of Eqs. (17) and (18) are expressed as

$$\int_K \mathbf{q} \cdot \mathbf{w} dA = \int_{\partial K} k\hat{T}\mathbf{w} \cdot \mathbf{n}^+ dl - \int_K kT\nabla \cdot \mathbf{w} dA, \quad (19)$$

$$\int_K \rho c_p \frac{\partial T}{\partial t} \cdot v dA = \int_{\partial K} \hat{\mathbf{q}}v \cdot \mathbf{n}^+ dl - \int_K \mathbf{q} \cdot \nabla v dA$$
$$- \int_K (\nabla \cdot \mathbf{q}_r) \cdot v dA, \quad (20)$$

where $\hat{T}$ and $\hat{\mathbf{q}}$ are given by

$$\hat{T} = \{T\} + \mathbf{C}_1[T], \hat{\mathbf{q}} = \{\mathbf{q}\} - \mathbf{C}_1[\mathbf{q}] - C_2[T], \quad (21)$$

where $\{T\}$, $[T]$, $\{\mathbf{q}\}$, and $[\mathbf{q}]$ are defined as

$$\{T\} = \tfrac{1}{2}(T^+ + T^-), [T] = (T^+ - T^-)\mathbf{n}^+,$$
$$\{\mathbf{q}\} = \tfrac{1}{2}(\mathbf{q}^+ + \mathbf{q}^-), [\mathbf{q}] = (\mathbf{q}^+ - \mathbf{q}^-)\mathbf{n}^+. \quad (22)$$

In Eq. (21), the terms $\mathbf{C}_1$ and C_2 are the stabilization parameters. The term $\mathbf{C}_1$ is a vector satisfying [35]

$$\mathbf{C}_1 \cdot \mathbf{n}^+ = \tfrac{1}{2}\text{sgn}(\mathbf{v} \cdot \mathbf{n}^+) = C_1, \quad (23)$$

where $\mathbf{v}$ is an arbitrary vector without zero components, such as $\mathbf{v} = [1, 1]^T$. The term $C_2 = kh^{-1}$, with h denoting the minimum element length.

At the boundary walls exposed to the Dirichlet boundary condition, the numerical fluxes take the forms

$$\hat{T} = T_w, \hat{\mathbf{q}} = \mathbf{q}^+ - C_2(T^+ - T_w)\mathbf{n}^+, \quad (24)$$

where T_w denotes the boundary temperature. By substituting Eqs. (21) and (22) into Eqs. (19) and (20) and utilizing the

Galerkin weighting scheme, one can get the DGFE discretization for the EBE as

$$\mathbf{E}\mathbf{q}_x = \mathbf{F}, \mathbf{E}\mathbf{q}_y = \mathbf{G}, \quad (25)$$

and

$$\mathbf{M}\dot{\mathbf{T}} = \mathbf{N}, \quad (26)$$

where $\mathbf{q}_x = [q_{x1}, q_{x2}, \ldots, q_{xn}]^T$, $\mathbf{q}_y = [q_{y1}, q_{y2}, \ldots, q_{yn}]^T$, $\dot{\mathbf{T}} = [\frac{\partial T_1}{\partial t}, \frac{\partial T_2}{\partial t}, \ldots, \frac{\partial T_n}{\partial t}]^T$, and the matrices $\mathbf{E}$, $\mathbf{F}$, $\mathbf{G}$, $\mathbf{M}$, and $\mathbf{N}$ are expressed as

$$\mathbf{E}_{ji} = \int_K \phi_i \phi_j dA, \quad (27)$$

$$\mathbf{F}_j = k\left[\sum_{i=1}^n \int_{\partial K} T_i^+ n_x \left(\frac{1}{2} + C_1\right)\phi_i \phi_j dl \right.$$
$$+ \sum_{i=1}^n \int_{\partial K} T_i^- n_x \left(\frac{1}{2} - C_1\right)\phi_i \phi_j dl$$
$$\left. - \sum_{i=1}^n \int_K T_i^+ \frac{\partial \phi_j}{\partial x}\phi_i dA \right], \quad (28)$$

$$\mathbf{G}_j = k\left[\sum_{i=1}^n \int_{\partial K} T_i^+ n_y \left(\frac{1}{2} + C_1\right)\phi_i \phi_j dl \right.$$
$$+ \sum_{i=1}^n \int_{\partial K} T_i^- n_y \left(\frac{1}{2} - C_1\right)\phi_i \phi_j dl$$
$$\left. - \sum_{i=1}^n \int_K T_i^+ \frac{\partial \phi_j}{\partial y}\phi_i dA \right], \quad (29)$$

$$\mathbf{M}_{ji} = \rho c_p \int_K \phi_i \phi_j dA, \quad (30)$$

$$\mathbf{N}_j = \sum_{i=1}^n \int_{\partial K} q_{xi}^+ n_x \left(\frac{1}{2} + C_1\right)\phi_i \phi_j dl + \sum_{i=1}^n \int_{\partial K} q_{xi}^- n_x \left(\frac{1}{2} - C_1\right)\phi_i \phi_j dl + \sum_{i=1}^n \int_{\partial K} q_{yi}^+ n_y \left(\frac{1}{2} + C_1\right)\phi_i \phi_j dl$$
$$+ \sum_{i=1}^n \int_{\partial K} q_{yi}^- n_y \left(\frac{1}{2} - C_1\right)\phi_i \phi_j dl - \sum_{i=1}^n \int_{\partial K} C_2\left(T_i^+ - T_i^-\right)\phi_i \phi_j dl - \sum_{i=1}^n \int_K q_{xi}^+ \frac{\partial \phi_j}{\partial x}\phi_i dA$$
$$- \sum_{i=1}^n \int_K q_{yi}^+ \frac{\partial \phi_j}{\partial y}\phi_i dA - \sum_{i=1}^n \int_K \nabla \cdot \mathbf{q}_{ri}\phi_i \phi_j dA, \quad (31)$$

where n_x and n_y are the components of the normal vector $\mathbf{n}^+$ in the x and y directions, respectively.

Then, by calculating the matrix elements in Eqs. (27)–(31), and solving Eqs. (25) and (26), one can obtain the variables $\mathbf{q}_x$, $\mathbf{q}_y$, and $\dot{\mathbf{T}}$ in the current element. The field solutions within the computational domain can then be depicted via the straightforward element-to-element sweep calculation.

D. Transient term discretization

The transient term is discretized by using a standard Euler forward difference scheme [17] as

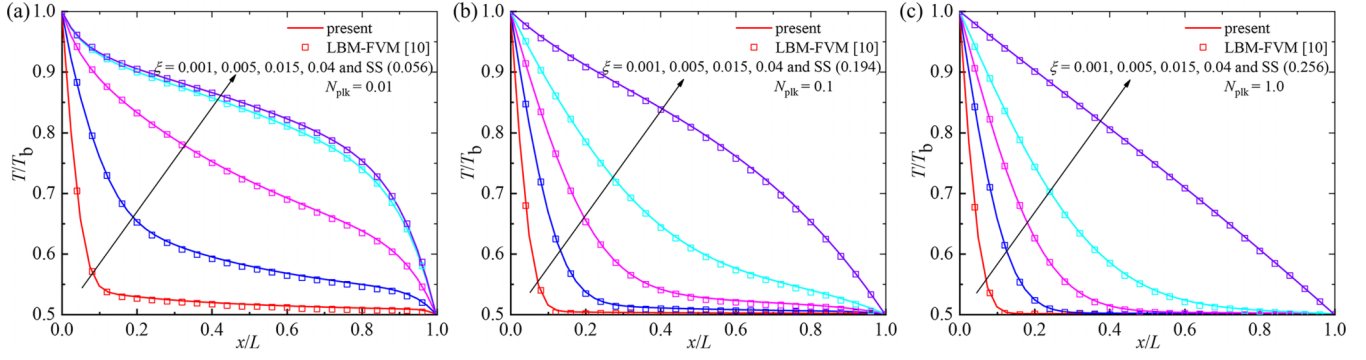$$\mathbf{T}^{t+\Delta t} = \dot{\mathbf{T}}^t \Delta t + \mathbf{T}^t, \quad (32)$$

FIG. 2. Temperature distribution in the planar medium with (a) $N_{\mathrm{plk}} = 0.01$, (b) $N_{\mathrm{plk}} = 0.1$, and (c) $N_{\mathrm{plk}} = 1.0$ at $\omega = 0$.

where $\mathbf{T} = [T_1, T_2, \ldots, T_n]^{\mathrm{T}}$, and Δt is the time step which satisfies the Courant-Friedrich-Lewy (CFL) criterion of [17]

$$\mathrm{CFL} = \frac{\alpha \Delta t}{h^2} < 0.5, \tag{33}$$

where $\alpha = k/\rho c_p$ is the thermal diffusivity.

So far, the DGFE discretization for the governing equation of CRC heat-transfer problems has been accomplished.

E. Solution procedure

Based on the spatial and time discretization, the DGFE framework can be applied to solve the CRC heat-transfer problems in a participating medium according to the following procedure:

Step 1: Mesh the spatial and angular domains. Initialize the temperature and radiation intensity.

Step 2: Solve the radiation intensity.

(a) According to the initial temperature and radiation intensity, the source term S can be obtained from Eq. (5).

(b) Global iteration. Calculate the radiative intensity I in the first direction for the first element by using Eq. (13), and go to the next element until the last one. Then go to the next direction and sweep the element until all discretized directions. For the boundary-connected elements, impose the boundary condition by Eq. (12).

(c) Update the source term according to the newly calculated radiative intensity.

(d) Repeat the global iteration until the convergence,

$$\frac{\|G_{\mathrm{new}} - G_{\mathrm{old}}\|}{\|G_{\mathrm{new}}\|} < 10^{-6}, \tag{34}$$

where $G = \int_{4\pi} I(\mathbf{r}, \mathbf{\Omega}) d\mathbf{\Omega}$ denotes the incident radiation, and the symbol $\|\ \|$ denotes the L_2 norm.

Step 3: Solve the temperature.

(a) Calculate the $\nabla \cdot \mathbf{q}_{\mathrm{r}}$ by using Eq. (2).

(b) Calculate the $\mathbf{q}$ from the initial temperature by using Eq. (25).

(c) Calculate the $\dot{\mathbf{T}}$ from $\mathbf{q}$ and $\nabla \cdot \mathbf{q}_{\mathrm{r}}$ by using Eq. (26), and impose the Dirichlet boundary condition at the boundary edges by using Eq. (24).

(d) Calculate the temperature $\mathbf{T}$ at the next time step using Eq. (32).

Step 4: Check if the system satisfies the steady-state (SS) criterion

$$\frac{\|T^{t+\Delta t} - T^t\|}{\|T^{t+\Delta t}\|} < 10^{-6}. \tag{35}$$

Step 5: If the temperature reaches the SS, end the calculation. Otherwise, return to Step 2.

III. RESULTS AND DISCUSSION

In this section, the present DGFE framework is applied to several cases, including the 1D planar medium and the 2D square medium, to evaluate its performance on CRC heat transfer. The physical parameters of the medium are assumed to be constant. For the transient calculations in all cases, the CFL number is set to 0.01 to determine the corresponding time step. All the simulations in this paper are implemented with MATLAB code and performed on a personal desktop with a configuration of AMD Ryzen 7-5800 processor with 3.40 GHz CPU and 16 GB RAM.

Some dimensionless parameters are used to facilitate the analysis and comparison. The conduction-radiation parameter that describes the ratio of heat conduction energy to radiation

TABLE I. Dimensionless temperature at $\xi = 0.05$ for the 1D medium with $N_{\mathrm{plk}} = 0.1$, $\omega = 0.5$, $T_0 = 0$.

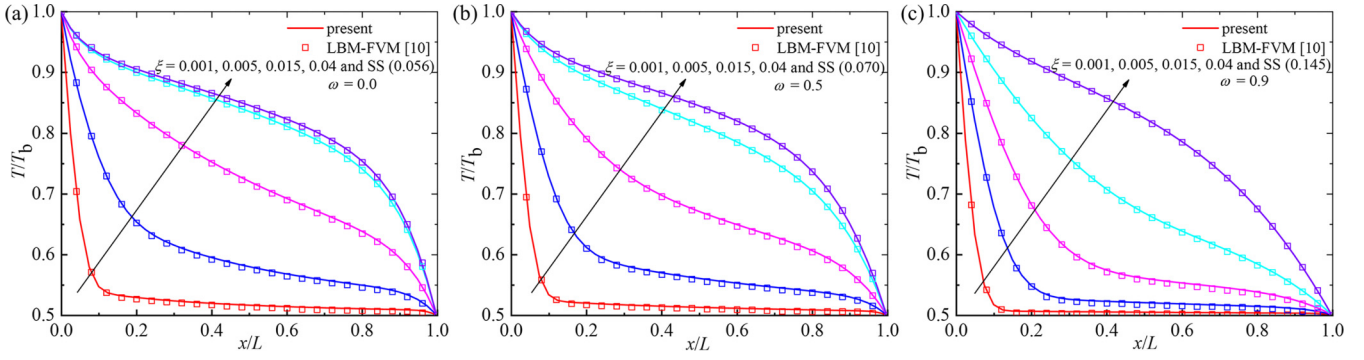|			Dimensionless temperature T/T_{b}		
ε_{W}	ε_{E}	Literature	$x/L = 0.25$	$x/L = 0.5$	$x/L = 0.75$
1.0	1.0	Tsai and Lin [36]	0.4889	0.1773	0.0588
		Talukdar and Mishra [8]	0.4892	0.1768	0.0585
		Mishra and Roy [10]	0.4897	0.1771	0.0587
		Mondal and Mishra [11]	0.4898	0.1769	0.0583
		Sun and Zhang [37]	0.4894	0.1771	0.0585
		Present	0.4896	0.1772	0.0586
1.0	0.0	Tsai and Lin [36]	0.5031	0.2001	0.0830
		Talukdar and Mishra [8]	0.5033	0.1995	0.0824
		Mishra and Roy [10]	0.4996	0.1991	0.0820
		Mondal and Mishra [11]	0.5025	0.1958	0.0800
		Sun and Zhang [37]	0.5028	0.1992	0.0823
		Present	0.5040	0.2004	0.0833

FIG. 3. Temperature distribution in the planar medium with (a) $\omega = 0.0$, (b) $\omega = 0.5$, and (c) $\omega = 0.9$ at $N_{\text{plk}} = 0.01$.

energy, i.e., the Planck number, is expressed as

$$N_{\text{plk}} = \frac{k\beta}{4\sigma T_{\text{b}}^3},\tag{36}$$

where T_{b} represents the characteristic temperature. The dimensionless time is used to represent the transient moments, and it is defined as

$$\xi = \alpha\beta^2 t.\tag{37}$$

In addition, the radiative heat flux and conductive heat flux are nondimensionalized by

$$Q_{\text{r}}^* = \frac{\mathbf{q}_{\text{r}}}{\sigma T_{\text{b}}^4}, \, Q_{\text{c}}^* = \frac{\mathbf{q}_{\text{c}}}{\sigma T_{\text{b}}^4},\tag{38}$$

where $\mathbf{q}_{\text{c}}$ is the conductive heat flux.

A. One-dimensional cases

The present DGFE framework is used to solve the 1D CRC heat-transfer problems and compared with other numerical results to verify its correctness. For the 1D planar participating medium, the initial temperature of the system is T_0. At time $t > 0$, the temperature of the west boundary ($x/L = 0$) suddenly rises to $T_{\text{b}}(> T_0)$ and then maintains, and the temperature of the east boundary ($x/L = 1.0$) remains constant at T_0. The medium has a thickness of $L = 1$ m and

an extinction coefficient of $\beta = 1 \, \text{m}^{-1}$. Under the combined impacts of radiation and conduction, the temperature of the medium will gradually increase until the steady state. The 1D plate is divided into 40 elements. As for the 1D planar medium, because of the azimuthal symmetry only the zenith space needs to be discretized, and it is discretized into 10 directions.

We first calculated the dimensionless temperature T/T_{b} for the case with $N_{\text{plk}} = 0.1$, $\omega = 0.5$, and $T_0 = 0$. Two pairs of boundary emissivities—$\varepsilon_{\text{W}} = 1.0$, $\varepsilon_{\text{E}} = 1.0$ and $\varepsilon_{\text{W}} = 1.0$, $\varepsilon_{\text{E}} = 0.0$—are considered.

Table I shows the present DGFE solutions of T/T_{b} at the dimensionless time $\xi = 0.05$, compared with available results at three points $x/L = 0.25$, 0.5, and 0.75. It is seen that the present results agree very well with those obtained via numerical results, indicating the excellent capability of the present DGFE framework for solving 1D CRC heat transfer. In terms of computational efficiency, the CPU time of the DGFE calculations is 21.5 and 21.8 s for the cases with $\varepsilon_{\text{E}} = 1.0$ and 0.0, respectively. With the same element, angular discretization, and time step, the CPU time of the traditional FEM for the same cases reads 29.1 and 30.3 s, which is even longer than that of the DGFE. The computational time comparison illustrates the computational efficiency of the present DGFE framework.
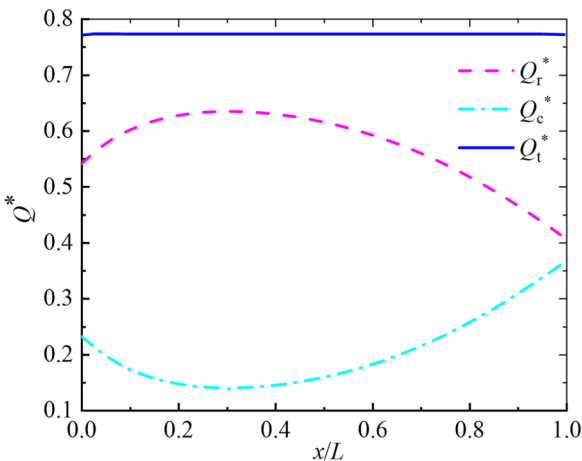

FIG. 4. The steady-state heat flux distribution in the planar medium at $N_{\text{plk}} = 0.1$ and $\omega = 0.0$.
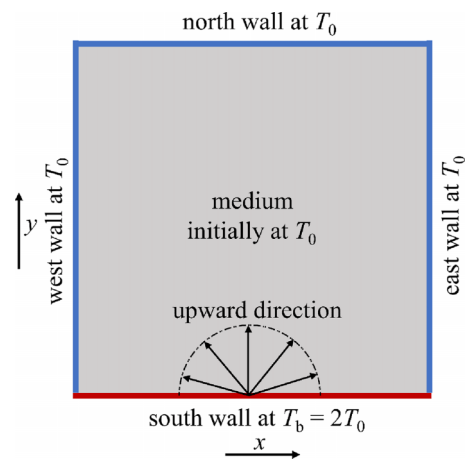

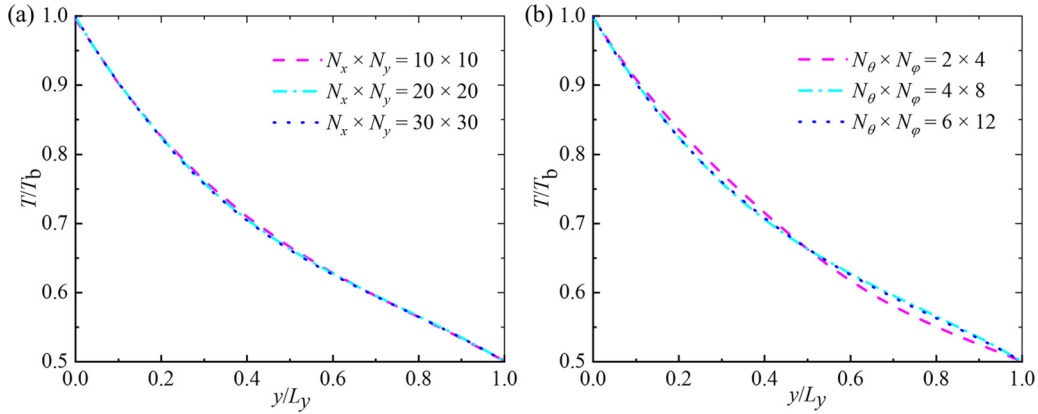FIG. 5. Physical model of the 2D square medium.

FIG. 6. Dimensionless temperature at the centerline $x/L_x = 0.5$ in the 2D isotropic media discretized by using different (a) spatial grids, (b) angular grids.

Further, by setting the boundary emissivity as $\varepsilon_E = \varepsilon_W = 1$, we plot the temperature distribution along the nonscattering medium at different time moments, obtained by the present DGFE in Fig. 2 for the cases with different $N_{plk} = 0.01$, 0.1, and 1.0. In this case, the initial temperature of the medium is kept at $T_0 > 0$. For $t > 0$, the west boundary is heated up and remains at $T_b = 2T_0$ while the east boundary maintains at T_0. The LBM-FVM solutions for the same case obtained by Mishra and Roy [10] are also plotted for reference. It is seen that the LBM-FVM and DGFE results are in great agreement for all the cases. Keeping in mind that the LBM-FVM used 100 lattices/control volumes, which is much more than the 40 elements in the present framework, one can confirm the good convergence and computational efficiency of the present DGFE framework. It is also observed that the temperature profiles are strongly nonlinear induced by the radiation effect, and the nonlinear trend becomes more striking for the smaller N_{plk} case with a stronger radiation effect. In addition, we can find that it takes more time to reach the steady state for the case with a larger N_{plk}. This is because the speed of radiative transfer is far greater than conduction.

When considering the medium scattering, we presented in Fig. 3 the temperature distribution along the medium with different scattering albedo $\omega = 0.0$, 0.5, and 0.9. The conduction-radiation parameter is set as $N_{plk} = 0.01$. As can be seen, results obtained via the LBM-FVM and the present

DGFE match closely for all cases. Due to the multiple scattering effects, the time to reach the steady state becomes longer for the case with a bigger scattering albedo.

The heat flux in the 1D planar medium at the steady state is also calculated. Figure 4 shows the dimensionless heat flux profile, including the radiative heat flux Q_r^*, conductive heat flux Q_c^*, and total heat flux $Q_t^* = Q_r^* + Q_c^*$, for the case with $N_{plk} = 0.1$ and $\omega = 0.0$. As can be seen, due to the high radiation intensity emitted from the hot west wall, the Q_r^* gradually increases from $x/L = 0$ and reaches its maximum at the location near $x/L = 0.3$, and then decreases gradually until the east wall at $x/L = 1.0$. In contrast, the conductive heat flux Q_c^* shows a completely opposite trend to the Q_r^* as the total heat flux Q_t^* at the steady state is constant for any locations. Results in Fig. 4 reveal the coupling effect of radiation and conduction, and they refer to the radiative and conductive heat flux for later research on this case.

B. Two-dimensional cases

As shown in Fig. 5, we consider the 2D medium with the length and width of $L_x = L_y = 1.0$ m. The medium has an extinction coefficient of $\beta = 1\,\mathrm{m}^{-1}$. The temperature of the medium is initially at $T_0 > 0$. At time $t > 0$, the south wall rises to $T_b = 2T_0$ and then maintains, while the other walls are
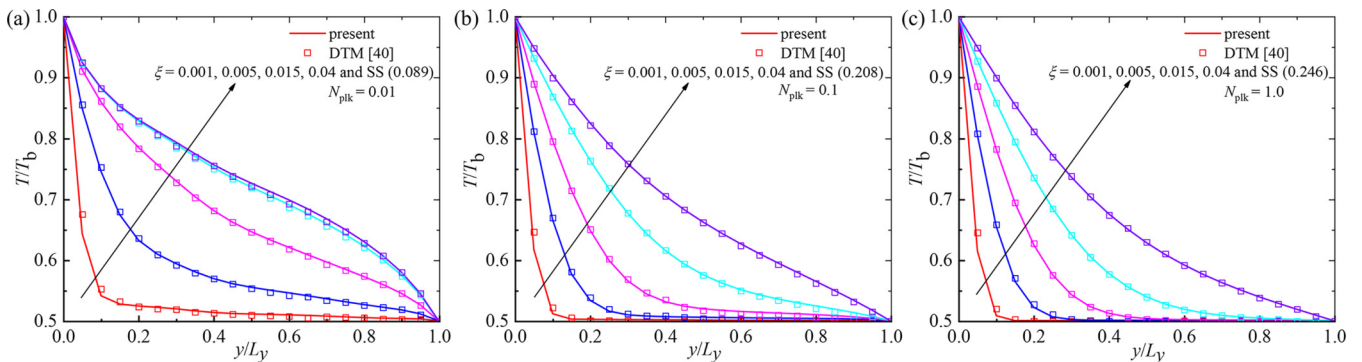

FIG. 7. Temperature distribution along the centerline of $x/L_x = 0.5$ in the 2D isotropical media with (a) $N_{plk} = 0.01$, (b) $N_{plk} = 0.1$, and (c) $N_{plk} = 1.0$ at $\varepsilon_S = 1.0$ and $\omega = 0.0$.
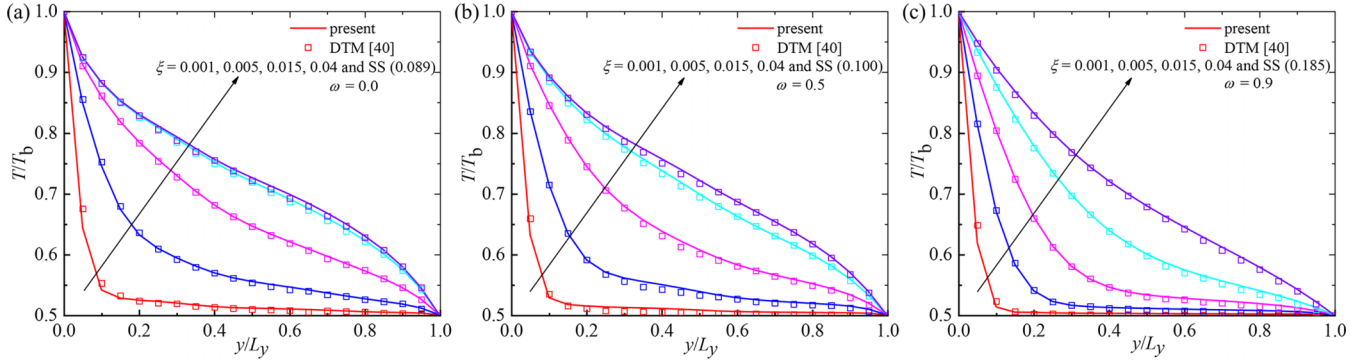
FIG. 8. Temperature distribution along the centerline of $x/L_x = 0.5$ in the 2D isotropical media with (a) $\omega = 0.0$, (b) $\omega = 0.5$, and (c) $\omega = 0.9$ at $\varepsilon_S = 1.0$ and $N_{plk} = 0.01$.

kept at T_0. The emissivity of the east, west, and north walls is kept at $\varepsilon_E = \varepsilon_W = \varepsilon_N = 1.0$.

1. Isotropic scattering

Here we consider a square enclosure filled with an absorbing, emitting, and isotropic scattering medium. The grid-independence tests for 2D cases are first carried out. At the angular discretization of $N_\theta \times N_\varphi = 4 \times 8$, Fig. 6(a) shows the steady-state temperature along the centerline $x/L_x = 0.5$ for the cases with different spatial grids of $N_x \times N_y = 10 \times 10$, 20×20, and 30×30. The other control parameters are set as $N_{plk} = 0.1$, $\omega = 0.0$, and $\varepsilon_S = 1.0$. It is found that consistent temperature distributions can be obtained even by using 10×10 grids. There is no appreciable difference between the results obtained from 20×20 grids and those obtained from 30×30 grids. Figure 6(b) depicts the effect of angular grid size on the temperature distribution at the fixed spatial grid of $N_x \times N_y = 20 \times 20$. As can be observed, the temperature obtained by using $N_\theta \times N_\varphi = 4 \times 8$ is almost the same as that by using $N_\theta \times N_\varphi = 6 \times 12$, indicating that $N_\theta \times N_\varphi = 4 \times 8$ is enough for angular discretization. Results in Fig. 6 prove that $N_x \times N_y = 20 \times 20$ spatial grids and $N_\theta \times N_\varphi = 4 \times 8$ angular grids are enough for obtaining solutions for the 2D CRC heat-transfer problems, and they are adopted in the following numerical calculations.

The DGFE solutions of the steady-state temperature at different locations of y/L_y along the perpendicular centerline of $x/L_x = 0.5$ are presented in Table II for the cases with $N_{plk} = 1.0$, 0.1, and 0.01, and they are compared with published data to verify the accuracy of the present framework. It is seen that the present results are in good agreement with the published data, illustrating the capability and accuracy of the present DGFE framework for 2D CRC heat-transfer problems. The CPU time of the DGFE calculation process reads 460.6, 1297.9, and 1460.4 s for the cases with $N_{plk} = 0.01$, 0.1, and 1.0, respectively, which is acceptable in practical applications.

Further, we plotted the temperature distribution along the perpendicular centerline at dimensionless time $\xi = 0.001$, 0.005, 0.015, 0.04, and steady state in Figs. 7 and 8 for the cases with varying N_{plk} and ω, respectively. All the DGFE results are compared with the DTM results [40]. For the cases with $\omega = 0.0$, $\varepsilon_S = 1.0$, and different $N_{plk} = 0.01$, 0.1, and 1.0, the temperature distributions are presented in Fig. 7. For

the cases with $\varepsilon_S = 1.0$, $N_{plk} = 0.01$, and different $\omega = 0.0$, 0.5, and 0.9, the temperature distributions are presented in Fig. 8. It is seen that the results obtained via two different numerical methods agree well with each other. The temperature changing trends in Figs. 7 and 8 are like those in Figs. 2 and 3 for the 1D cases, respectively. Nevertheless, the steady-state temperature in the 2D media is much lower than that in the 1D cases, especially at the central region of the medium. This is because in the 2D media, heat energy will spread to the west and east directions when propagating to the north from the hot south wall.

At the fixed $N_{plk} = 0.01$ and $\omega = 0.0$, the temperature distributions at $\xi = 0.015$ and steady time for the cases with $\varepsilon_S = 1.0$, 0.5, and 0.1 are compared in Figs. 9(a) and 9(b), respectively, to highlight the effects of the hot wall. For the case with a lower ε_S, because the thermal emission from the hot boundary is less and more incoming radiation will be reflected, the temperature decreases faster and remains lower than that with higher ε_S, as shown in Fig. 9. Due to the same reason, the dimensionless steady-state time, 0.089, 0.090, and 0.096 for the case with $\varepsilon_S = 1.0$, 0.5, and 0.1, respectively, is later for the case with a lower ε_S.

2. Anisotropic scattering

The present DGFE framework is extended to solve the CRC heat-transfer problems in a 2D square enclosure filled with an anisotropically scattering medium. The forward and

TABLE II. Steady-state temperature at different locations of y/L_y along the perpendicular centerline of $x/L_x = 0.5$.

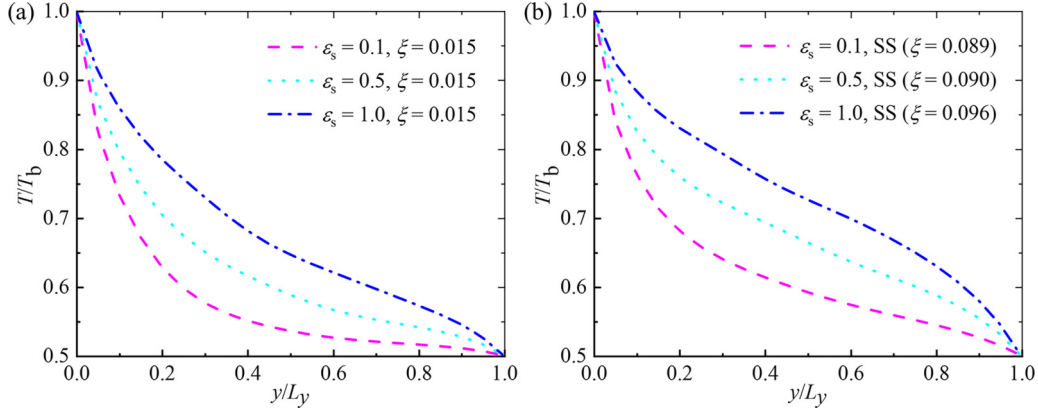| N_{plk}	Location of y/L_y	Wu [38]	Yuen [39]	Mondal [11]	Wei [14]	Present
1.0	0.3	0.733	0.737	0.738	0.738	0.738
	0.5	0.630	0.630	0.631	0.631	0.632
	0.7	0.560	0.560	0.565	0.564	0.564
0.1	0.3	0.760	0.763	0.761	0.759	0.760
	0.5	0.663	0.661	0.664	0.662	0.663
	0.7	0.590	0.589	0.596	0.593	0.592
0.01	0.3	0.791	0.807	0.777	0.788	0.792
	0.5	0.725	0.726	0.722	0.722	0.727
	0.7	0.663	0.653	0.672	0.662	0.661

FIG. 9. Temperature distribution along the centerline of $x/L_x = 0.5$ in the 2D medium with different emissivities of the south wall, $N_{plk} = 0.01$ and $\omega = 0.0$.

backward scattering media are considered, respectively. The scattering phase function for the forward scattering is given by

$$\Phi(\mathbf{\Omega}^{m'}, \mathbf{\Omega}^m) = 1 + \mathbf{\Omega}^{m'} \cdot \mathbf{\Omega}^m \tag{39}$$

and that for the backward scattering is given by

$$\Phi(\mathbf{\Omega}^{m'}, \mathbf{\Omega}^m) = 1 - \mathbf{\Omega}^{m'} \cdot \mathbf{\Omega}^m. \tag{40}$$

At the fixed control parameters of $\omega = 0.5$, $N_{plk} = 0.01$, and $\varepsilon_S = 1.0$, we present in Table III the steady-state temperature at specific points along the centerline of $x/L_x = 0.5$ in isotropically and anisotropically scattering media, respectively. It can be concluded that the scattering pattern influences the temperature distribution in a slight manner. In the forward scattering medium, the temperature near the hot south wall is the lowest as more radiation is scattered into the north direction. As a result, the temperature near the north wall is the highest as more radiation energy propagates to this boundary.

For the media with different scattering patterns, we further compare the steady-state heat flux, including the radiative heat flux and conductive heat flux along the perpendicular centerline of $x/L_x = 0.5$ in Figs. 10(a) and 10(b), respectively. As seen from Fig. 10(a), the forward scattering enhances the radiative heat flux, and this phenomenon can be interpreted as follows. For the forward scattering medium, the radiation intensity along the upward direction is enhanced compared with that for the isotropically scattering medium. As a result, the radiative heat flux with an upward direction is enhanced. In contrast, the backward scattering shows a suppression impact on the radiative heat flux. The distributions of conductive heat

flux for media with different scattering patterns, plotted in Fig. 10(b), are quite close, indicating that conductive heat flux is less affected by the scattering pattern. The conductive heat flux is determined by the temperature other than the radiation intensity, which is directly influenced by the medium scattering events.

IV. CONCLUSIONS

In this work, a unified DGFE framework is proposed to solve the transient CRC heat-transfer problems. Both the RTE and the EBE are solved based on the DGFE discretization. The second-order EBE is rearranged as two first-order equations to match the DGFE solution domain. The proposed DGFE is applied to solve the CRC heat-transfer problems in 1D planar and 2D square geometries filled with absorbing, emitting, and scattering media. The DGFE solutions of temperature distributions are obtained and their comparisons with published data verify the accuracy of the present DGFE framework. Based on the DGFE results, it is found that big conduction-radiation parameter, high scattering albedo, and low wall emissivity will increase the time for the CRC heat transfer to reach the steady state. Further, the impacts of the medium scattering pattern on the CRC heat-transfer problems in 2D anisotropic scattering media are also studied. Results indicate that the scattering pattern has an obvious influence on the radiative heat flux while it has little impact on conductive heat flux. The proposed framework can be extended straightforwardly to CRC heat-transfer problems in complex media for highly accurate solutions on a unified DGFE discretization.

TABLE III. Steady-state dimensionless temperature along the centerline $x/L_x = 0.5$ with different scattering patterns.

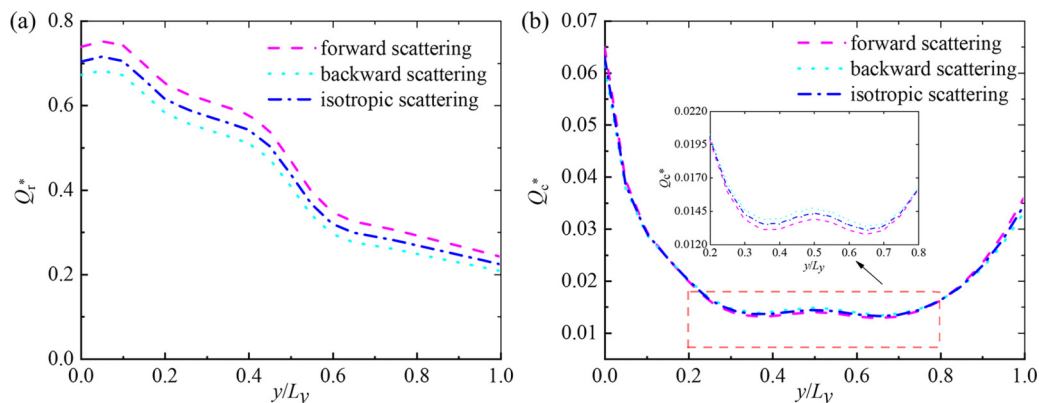| Location of y/L_y	Dimensionless temperature T/T_b		
	forward scattering	isotropic scattering	backward scattering
0.1	0.892	0.894	0.896
0.3	0.789	0.791	0.793
0.5	0.722	0.722	0.722
0.7	0.657	0.654	0.652
0.9	0.573	0.571	0.569

FIG. 10. Steady-state (a) radiative heat flux and (b) conductive heat flux along the centerline of $x/L_x = 0.5$ in 2D media with different scattering patterns.

[1] R. Viskanta and E. D. Hirleman, Combined conduction-radiation heat transfer through an irradiated semitransparent plate, J. Heat Transf. **100**, 169 (1978).

[2] R. Viskanta and F. P. Incropera, Combined conduction and radiation heat transfer in porous materials heated by intense solar radiation, J. Sol. Energy Eng. **107**, 29 (1985).

[3] F. Asllanaj, G. Jeandel, J. R. Roche *et al.*, Transient combined radiation and conduction heat transfer in fibrous media with temperature and flux boundary conditions, Int. J. Therm. Sci. **43**, 939 (2004).

[4] J. R. Thomas, Jr., Coupled radiation/conduction heat transfer in ceramic liners for diesel engines, Numer. Heat Transf. Part A **21**, 109 (1992).

[5] J. F. Luo, S. L. Chang, J. K. Yang *et al.*, Conduction and radiation in a rectangular isotropic scattering medium with black surfaces by the RTNAM, Int. J. Heat Mass Transf. **52**, 5064 (2009).

[6] R. Viskanta and R. J. Grosh, Heat transfer by simultaneous conduction and radiation in an absorbing medium, J. Heat Transf. **84**, 63 (1962).

[7] R. Viskanta and R. J. Grosh, Effect of surface emissivity on heat transfer by simultaneous conduction and radiation, Int. J. Heat Mass Transf. **5**, 729 (1962).

[8] P. Talukdar and S. C. Mishra, Transient conduction and radiation heat transfer with heat generation in a participating medium using the collapsed dimension method, Numer. Heat Transf. Part A **39**, 79 (2001).

[9] S. C. Mishra and A. Lankadasu, Transient conduction-radiation heat transfer in participating media using the lattice Boltzmann method and the discrete transfer method, Numer. Heat Transf. Part A **47**, 935 (2005).

[10] S. C. Mishra and H. K. Roy, Solving transient conduction and radiation heat transfer problems using the lattice Boltzmann method and the finite volume method, J. Comput. Phys. **223**, 89 (2007).

[11] B. Mondal and S. C. Mishra, Application of the lattice Boltzmann method and the discrete ordinates method for solving transient conduction and radiation heat transfer problems, Numer. Heat Transf. Part A **52**, 757 (2007).

[12] M. M. Razzaque, J. R. Howell, and D. E. Klein, Coupled radiative and conductive heat transfer in a two-dimensional rectangular enclosure with gray participating media using finite elements, J. Heat Transf. **106**, 613 (1984).

[13] J. M. Zhao and L. H. Liu, Spectral element approach for coupled radiative and conductive heat transfer in semitransparent medium, J. Heat Transf. **129**, 1417 (2007).

[14] Y. J. Wei, X. C. Liu, K. Y. Zhu *et al.*, A unified lattice Boltzmann framework for combined radiation-conduction heat transfer, Int. J. Heat Mass Transf. **200**, 123513 (2023).

[15] Y. Zhang, H. L. Yi, and H. P. Tan, Natural element method analysis for coupled radiative and conductive heat transfer in semitransparent medium with irregular geometries, Int. J. Therm. Sci. **76**, 30 (2014).

[16] W. H. Reed and T. R. Hill, Triangular mesh methods for the neutron transport equation, Los. Alamos Sci. Lab. Rep. No. LA-UR-73-479 (1973), https://www.osti.gov/biblio/4491151.

[17] B. Q. Li, *Discontinuous Finite Elements in Fluid Dynamics and Heat Transfer* (Springer, London, 2006).

[18] A. Dedner, B. Kane, R. Klöfkorn *et al.*, Python framework for hp-adaptive discontinuous Galerkin methods for two-phase flow in porous media, Appl. Math. Model. **67**, 179 (2019).

[19] J. G. Liu and C. W. Shu, A high-order discontinuous Galerkin method for 2D incompressible flows, J. Comput. Phys. **160**, 577 (2000).

[20] C. E. Baumann and J. T. Oden, A discontinuous hp finite element method for convection-diffusion problems, Comput. Methods Appl. Mech. Eng. **175**, 311 (1999).

[21] Q. Xu and J. S. Hesthaven, Discontinuous Galerkin method for fractional convection-diffusion equations, SIAM J. Numer. Anal. **52**, 405 (2014).

[22] X. Cui and B. Q. Li, A discontinuous finite-element formulation for internal radiation problems, Numer. Heat Transf. Part B **46**, 223 (2004).

[23] X. Cui and B. Q. Li, A discontinuous finite-element formulation for multidimensional radiative transfer in absorbing, emitting, and scattering media, Numer. Heat Transf. Part B **46**, 399 (2004).

[24] L. H. Liu and L. J. Liu, Discontinuous finite element method for radiative heat transfer in semitransparent graded index medium, J. Quant. Spectrosc. Radiat. Transf. **105**, 377 (2007).

[25] D. Kitzmann, J. Bolte, and A. B. C. Patzer, Discontinuous Galerkin finite element methods for radiative transfer in spherical symmetry, Astron. Astrophys. **595**, A90 (2016).

[26] P. Clarke, H. Wang, J. Garrard *et al.*, Space-angle discontinuous Galerkin method for plane-parallel radiative transfer equation, J. Quant. Spectrosc. Radiat. Transf. **233**, 87 (2019).

[27] Y. Y. Feng and C. H. Wang, Discontinuous finite element method with a local numerical flux scheme for radiative transfer with strong inhomogeneity, Int. J. Heat Mass Transf. **126**, 783 (2018).

[28] M. Ghattassi, J. R. Roche, F. Asllanaj *et al.*, Galerkin method for solving combined radiative and conductive heat transfer, Int. J. Therm. Sci. **102**, 122 (2016).

[29] C. H. Wang, Y. Y. Feng, K. Yue *et al.*, Discontinuous finite element method for combined radiation-conduction heat transfer in participating media, Int. Commun. Heat Mass Transf. **108**, 104287 (2019).

[30] B. Cockburn and C. W. Shu, The local discontinuous Galerkin time-dependent method for convection-diffusion systems, SIAM J. Numer. Anal. **35**, 2440 (1998).

[31] B. Cockburn and C. W. Shu, Runge-Kutta discontinuous Galerkin methods for convection-dominated problems, J. Sci. Comput. **16**, 173 (2001).

[32] P. Castillo, A review of the local discontinuous Galerkin (LDG) method applied to elliptic problems, Appl. Numer. Math. **56**, 1307 (2006).

[33] M. F. Modest and S. Mazumder, *Radiative Heat Transfer* (Academic Press, San Diego, 2021).

[34] P. D. Lax, Weak solutions of nonlinear hyperbolic equations and their numerical computation, Commun. Pure Appl. Math. **7**, 159 (1954).

[35] B. Cockburn and B. Dong, An analysis of the minimal dissipation local discontinuous Galerkin method for convection–diffusion problems, J. Sci. Comput. **32**, 233 (2007).

[36] J.-H. Tsai and J.-D. Lin, Transient combined conduction and radiation with anisotropic scattering, J. Thermophys. Heat Transf. **4**, 92 (1990).

[37] Y. Sun and X. Zhang, Analysis of transient conduction and radiation problems using lattice Boltzmann and finite volume methods, Int. J. Heat Mass Transf. **97**, 611 (2016).

[38] C. Y. Wu and N. R. Ou, Transient two-dimensional radiative and conductive heat-transfer in a scattering medium, Int. J. Heat Mass Transf. **37**, 2675 (1994).

[39] W. W. Yuen and E. E. Takara, Analysis of combined conductive-radiative heat-transfer in a two-dimensional rectangular enclosure with a gray medium, J. Heat Transf. Trans. ASME **110**, 468 (1988).

[40] S. C. Mishra, P. Talukdar, D. Trimis *et al.*, Computational efficiency improvements of the radiative transfer problems with or without conduction—-a comparison of the collapsed dimension method and the discrete transfer method, Int. J. Heat Mass Transf. **46**, 3083 (2003).